Design and investigation of de Vries liquid crystals based on 5-phenyl-pyrimidine and (*R*,*R*)-2,3-epoxyhexoxy backbone

S. P. Sreenilayam,[1] D. Rodriguez-Lojo,[2] V. P. Panov,[1] V. Swaminathan,[1] J. K. Vij,[1,*] Yu. P. Panarin,[1,3] E. Gorecka,[4] A. Panov,[2] and P. J. Stevenson[2]

[1]*Department of Electronic and Electrical Engineering, Trinity College Dublin, The University of Dublin, Dublin 2, Ireland*
[2]*School of Chemistry and Chemical Engineering, Queens University, Belfast BT7 1NN, United Kingdom*
[3]*School of Electrical and Electronic Engineering, Dublin Institute of Technology, Dublin 8, Ireland*
[4]*Department of Chemistry, Warsaw University, Al. Zwirki i Wigury 101, 02089 Warsaw, Poland*

(Received 13 July 2017; revised manuscript received 1 September 2017; published 3 October 2017)

Calamitic liquid crystals based on 5-phenyl-pyrimidine derivatives have been designed, synthesized, and characterized. The 5-phenyl pyrimidine core was functionalized with a chiral (*R*,*R*)-2,3-epoxyhexoxy chain on one side and either siloxane or perfluoro terminated chains on the opposite side. The one involving a perfluorinated chain shows SmA^* phase over a wide temperature range of 82 °C, whereas the siloxane analog exhibits both SmA^* and SmC^* phases over a broad range of temperatures, and a weak first-order SmA^*-SmC^* transition is observed. For the siloxane analog, the reduction factor for the layer shrinkage R (relative to its thickness at the SmA^*-SmC^* transition temperature, T_{AC}) is ∼0.373, and layer shrinkage is 1.7% at a temperature of 13 °C below the T_{AC}. This compound is considered to have "de Vries smectic" characteristics with the de Vries coefficient C_{deVries} of ∼0.86 on the scale of zero (maximum-layer shrinkage) to 1 (zero-layer shrinkage). A three-parameter mean-field model is introduced for the orientational distribution function (ODF) to reproduce the electro-optic properties. This model explains the experimental results and leads to the ODF, which exhibits a crossover from the sugar-loaf to diffuse-cone ODF some 3 °C above T_{AC}.

DOI: 10.1103/PhysRevE.96.042701

I. INTRODUCTION

Chiral smectic liquid crystals (LCs) with mesophases close to room temperature are extremely useful for the next generation of displays and electro-optical devices. The devices based on ferroelectric smectics with extremely fast switching time (μs) compared to the currently used slowly switching nematics (ms) are very promising [1]. However, to obtain defect-free alignment in an LC cell over a broad range of temperatures, a prerequisite of zero or a small layer shrinkage for practical applications is required, the achievement of which is still an open challenge. In principle, one is able to align the material reasonably well in the nematic or smectic A phases. However, on a phase transition from SmA to SmC, a tilt emerges whereby the molecular long axis $\boldsymbol{n}$ tilts relative to the layer normal $\boldsymbol{z}$ by an angle θ that varies with temperature [Fig. 1(a)]. Consequently, the layer spacing (d_C) in the SmC phase decreases by a factor of cos θ provided liquid crystalline molecules are close enough to being considered as rigid rods. The layer shrinkage arising from the tilt together with surface anchoring of molecules leads to chevron structure(s) formed in the cell. These structures with opposite fold directions create zigzag defects at the interface in between the two oppositely folded chevrons. The emergence of these defects is an impediment to a successful commercialization of devices based on ferroelectric LCs [2–4]. The solution is therefore focused on developing chiral LCs with a minimal or zero-layer shrinkage at the SmA^*-SmC^* transition temperature and within the temperature range of SmC^* as well [4]. It is normally the case that where the layer shrinkage is much lower than the scaling factor, cos θ, the smectic phases of such compounds emerge from what are known as "de Vries smectics" [Fig. 1(b)].

A dozen or so compounds have been identified as having de Vries characteristics to varying degrees of perfection. According to the semiqualitative studies carried out so far, the calamitic LCs that combine a low orientational order parameter but large lamellar orderings are likely to exhibit better de Vries–type characteristics [5–9]. Most of the de Vries smectics contain trisiloxane or carbosilane backbones and perfluorinated side chains on either ends of the core; these terminations strongly promote lamellar orderings [10]. In this case, the alkane chains were replaced by an epoxy group (a precursor in the synthesis of the difluoro material). To obtain a large P_S in the SmC^* phase, it is pertinent to prepare highly enantiomeric enriched chiral molecules to avoid the cancelation effects of the oppositely handed enantiomers. In the literature, excellent protocols are given for preparing epoxides from allylic alcohols with large enantiomeric excesses [11]. However, to our knowledge, materials with enantiomeric enriched 5-phenyl pyrimidine epoxides have not yet been reported to have de Vries–like behavior [12]. The epoxide group may induce large electrical polarization. However, 5-phenyl pyrimidine is used extensively as an aromatic core in the synthesis of compounds that exhibit de Vries–like characteristics in chiral and nonchiral mesogens [13–15]. With this concept in mind, two new chiral materials containing epoxides in their structures have been designed, synthesized, and investigated.

In this article, we report the synthesis and properties of the two 5-phenyl pyrimidine derivatives that contain the chiral (R, R)-2,3-epoxyhexoxy chain in conjunction with trisiloxane (adpc042) or perfluorinated (DR257) terminal chains (see the Appendix for the synthetic procedure). Both moieties are therefore structurally related to each other, and both use the same aromatic core and epoxide chiral chain.

*jvij@tcd.ie

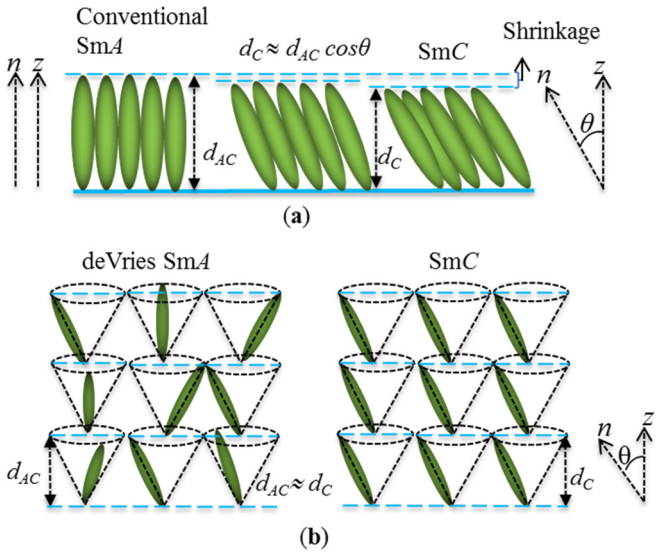

FIG. 1. Schematic representation of the molecular arrangements in the Sm*A* and Sm*C* mesophases as per (a) the conventional rigid-rod model and (b) the de Vries diffuse cone model [16]. z is the layer normal, $\boldsymbol{n}$ is the molecular long axis orientation, θ is the angle between $\boldsymbol{n}$ and z, and d_C and d_A are the layer spacing in Sm*C* and Sm*A*, respectively.

In DR257, the siloxane group is replaced with perfluorinated butane as an aliphatic linkage of six carbons with the aromatic core. A modification of the chain ending could have a significant effect on the properties, and with the objective of finding its effect on the electro-optic properties, we decided to explore this further to establish a well-desired structure-property relationship. The mesophases formed by these compounds were characterized by differential scanning calorimetry (DSC), polarized optical microscopy (POM), x-ray diffraction (XRD), electro-optics, and dielectric spectroscopy. Characterization of the LCs shows that the perfluorinated epoxide DR257 exhibits a stable SmA^* phase over a broad range of temperatures, whereas the siloxane-terminated analog adpc042 exhibits both SmA^* and SmC^* phases over a reasonably wide range of temperatures. In this trisiloxane compound, we achieve a layer shrinkage of 1.7% at a temperature of −13 °C below the SmA^*-SmC^* transition temperature. Since adpc042 LC exhibits both SmA^* and SmC^* phases, the properties of this compound are detailed below.

II. EXPERIMENT

The phase sequence and the transition temperatures were found by DSC thermograms (Perkin-Elmer DSC-7 calorimeter). The experiment was carried out under cooling at a rate of 10 °C min^{-1}. The electro-optical studies of the LCs were conducted using planar-aligned cells with parallel rubbed polyimide alignment layer KSRP-XX/D611P6NSS05. These cells were purchased from EHC, Japan. LC cells were studied by POM and electro-optics. An Olympus BX 52 equipped with a rotating table was used. The hot stage was fixed onto the rotating table. The hot stage was connected to a temperature controller, Eurotherm 2604. XRD measurements were carried out on a Bruker D8 diffractometer using a Cu $K\alpha$ source with a wavelength 0.154 nm. Dielectric spectroscopic studies were performed using an alpha high-resolution dielectric analyzer (Novocontrol GmbH, Germany) in the frequency range 1 Hz–10 MHz. Indium tin oxide (ITO) coated glass substrates were used to make cells for studies of the real and imaginary parts of the dielectric permittivity. Substrates were coated with RN 1175 polymer (Nissan Chemicals, Japan) to obtain the planar alignment. The cell thickness (d) was controlled by Mylar spacers. An ultraviolet-visible (uv-vis) spectrometer (Avaspec-2048) was used to measure d through interference fringes. The ITO sheet resistance of the substrates (20 Ω/□) is low enough to shift the peak frequency for the resistance of the ITO in series with the cell, beyond the experimental window of measurements. The dielectric spectra were recorded using the Novocontrol WINDETA program.

III. RESULTS AND DISCUSSIONS

A. Differential scanning calorimetry and polarizing optical microscopic studies

The molecular structure and the transition temperatures of siloxane pyrimidine adpc042 and the fluorinated pyrimidine DR257 are given in Figs. 2(a) and 2(b) (synthetic procedures are given in the Appendix). The result of a DSC thermogram of DR257 is given in Fig. 2(c). Here two transitions with enthalpies ΔH of ∼17.2 Jg^{-1} and ∼30.4 Jg^{-1} at temperatures of ∼143 °C and ∼56 °C are recorded. To identify the mesophases, textures of a 9 μm planar-aligned cell filled with DR257 are recorded with POM. Images corresponding to the two mesophases are shown in the inset of Fig. 2(c). Upon cooling from the isotropic temperature, the mesophase grows from a typical "batonnet" structure to a focal conic texture. Both the focal conic and the dark homeotropic textures obtained by POM are characteristics of the SmA^* phase [17]. Textures confirm that the phase transition from SmA^* to a crystalline state is at a temperature of 56 °C.

A representative of the DSC plot of adpc042 LC under cooling exhibits two peaks [Fig. 2(d)]. Both DR257 and adpc042 show the first-order Iso-SmA^* transition with ΔH of ∼11.71 Jg^{-1} and ∼17.2 Jg^{-1} occurring at temperatures of ∼82 °C and ∼145 °C. This is confirmed by POM where the focal conic fan-shaped texture from a 9 μm planar-aligned cell [Fig. 2(d) inset] is recorded. Upon lowering the temperature, the sample undergoes a weak first-order SmA^*-SmC^* transition with ΔH of ∼0.49 Jg^{-1} (0.069 kcal mol^{-1}) at 58 °C [12,18]. For a conventional SmA^*-SmC^* transition where the tilt angle stays at almost zero value in the SmA^* phase down to the transition temperature T_{AC}, the DSC thermogram exhibits a second-order transition with a step in the baseline without a peak being observed for the enthalpy of transition [19]. The SmC^* phase of adpc042 is distinguishable from SmA^* by POM where a fan-shaped texture from a planar-aligned cell is altered to a broken fan-shaped one [inset, Fig. 2(d)]. The dark homeotropic texture is changed to a Schlieren texture upon the transition from SmA^* to SmC^*. The entire replacement of trisiloxane in adpc042 by a tetrafluorocarbon chain in DR257 radically alters the mesomorphic behavior. The temperature range of SmA^* is increased from 23 °C to 89 °C, whereas SmC^* disappears. An increased temperature range of the SmA^* phase in DR257 could be due to a large dipole moment associated with the

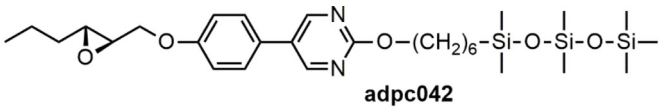

Cr -5 °C Sm*C** 58 °C Sm*A** 82 °C Iso

(a)

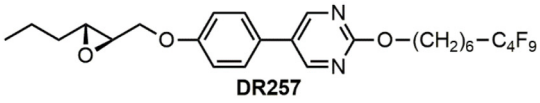

Cr 60 °C Sm*A** 152 °C Iso

(b)

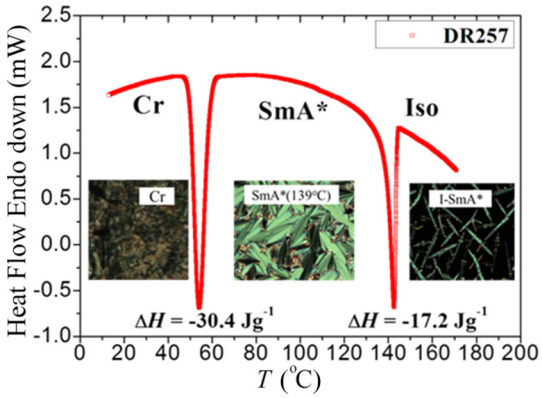

(c)

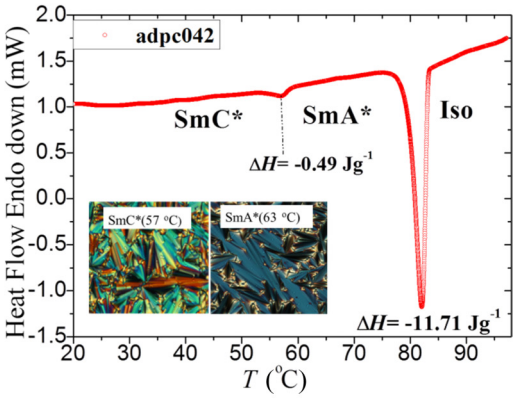

(d)

FIG. 2. Molecular structures and the DSC thermograms of adpc042 [(a) and (d)] and DR257 [(b) and (c)] are given. The phase-transition temperatures are obtained under the cooling cycle with a quasiequilibrium condition at the rate of ∼1 °C min^{-1} using POM. The cooling curves of the DSC thermograms are obtained at the rate of 10 °C min^{-1}. Iso denotes isotropic phase, while Cr denotes crystalline state. Insets in these two figures are the POM images of the mesophases seen under the crossed polarizers. Textures are recorded for a 9 μm planar-aligned cell in the cooling run.

fluorinated tail [20]. The siloxane groups in adpc042 enhance the thermal stability of the compound as well as lower the phase-transition temperatures. These features may be of great importance from the point of view of the molecular design and applications.

The POM images of a planar-aligned cell of thickness 9 μm filled with adpc042 recorded at 63 °C (∼19 °C below the Iso-Sm*A** transition temperature and 5 °C above the T_{AC}) are given in Fig. 3. The rubbing direction $\boldsymbol{R_d}$ is fixed at an angle $\alpha = \sim 15^{\circ}$ to the polarizer **P**.

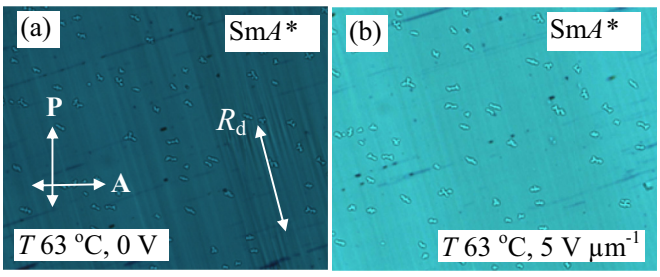

FIG. 3. POM images of the Sm*A** phase at a temperature of 63 °C in a 9 μm planar-aligned cell filled with adpc042 LC: (a) 0 V and (b) 5 V μm^{-1} (square wave AC electric field of 110 Hz applied).

The electric-field treatment of the LC cell gives rise to a uniform monodomain texture (Fig. 3(a)). An application of the external electric field across a cell in the well-aligned Sm*A** phase produces a change in the color of the texture [compare Figs. 3(a) and 3(b)] due to an increase in the birefringence Δn with the field, a characteristic of the de Vries behavior. In this phase, the molecules are tilted but are azimuthally disordered. The electric field produces a bias in the azimuthal distribution, and the molecules tilt in a particular direction determined by the polarity of the field. The resulting Sm*A** is reduced to the same symmetry as the Sm*C** phase through azimuthal ordering of the already tilted liquid crystalline molecules.

B. X-ray diffraction

Figure 4(a) shows the temperature dependence of the smectic-layer spacing determined by the XRD experiment. Upon cooling the sample below the isotropic phase, the layer spacing in the Sm*A** phase initially increases linearly with decreasing temperature. Upon approaching the Sm*A**- Sm*C** transition temperature, the thickness reverses its trend within Sm*A** from an increase to a decrease due to an emergence of the molecular tilt even in the Sm*A** phase. Upon further cooling of the sample cell, the layer thickness in the Sm*C**

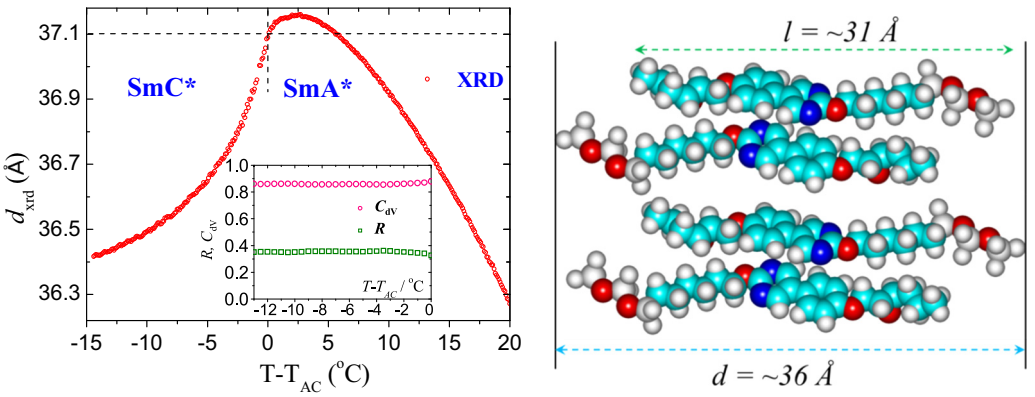

(a) (b)

FIG. 4. (a) Temperature dependence of the smectic layer spacing determined by XRD relative to the layer thickness at the SmA^* to SmC^* transition temperature. The inset shows plots of the de Vries coefficient C_{deVries} (□) and the reduction factor R (○) vs the reduced temperature $(T-T_{\text{AC}})$. de Vries characteristics are defined in terms of C_{deVries} and R. Measurements are carried out on a compound adpc042. (b) The simulated molecular structures of the compound adpc042.

phase continues to decrease much more slowly than expected from a conventional smectic, in which the layer thickness scales as cos θ. Figure 4(b) shows the simulated molecular structures of the compound adpc042 using the HYPERCHEM program. The simulated length l of the molecule is ~31 Å. A possible molecular arrangement in layers is shown in Fig. 4(b) such that the total length of a pair of molecules could be larger than the smectic-layer thickness.

A layer shrinkage of 1.7% is calculated from the XRD at a temperature of 13 °C below the SmA^*-SmC^* transition temperature T_{AC}. The layer shrinkage therefore is small. The behavior is similar to that in the SmA^* phase where the molecular directors in the SmA^* phase are distributed onto a cone where the azimuthal angle is degenerated. At the SmA^*- SmC^* transition, the tilt directions condense to within narrower limits, hence the disorder in the azimuthal angle disappears in the SmC^* phase. This process in itself requires no change in the layer thickness.

The reduction factor $R(T)$ of a smectic LC at temperature T is defined as

$$R(T) = \frac{\delta(T)}{\theta_{\text{opt}}(T)} = \frac{\cos^{-1}[d_C(T)/d_{\text{AC}}(T = T_{\text{AC}})]}{\theta_{\text{opt}}(T)}, \qquad (1)$$

where $\delta(T)$ governs the layer thickness at a temperature T within the SmC^* phase relative to the layer thickness at the SmA^*-SmC^* transition temperature, d_{AC}, upon assuming that the rigid rod model is applicable to the LC under investigation [21]. $\theta_{\text{opt}}(T)$ is the optical tilt angle determined by the POM at a temperature T (Fig. 5(a)). According to Eq. (1), an ideal de Vries smectic with $d_c(T) \approx d_{\text{AC}}(T = T_{\text{AC}})$ [Fig. 1(b)] produces a defect-free bookshelf geometry in the SmC^* phase with a reduction factor $R = 0$, i.e., the short-range molecular tilt order at a lower temperature in the SmA^* phase becomes long-range close to the SmA^*-SmC^* transition temperature, where the maximum de Vries cone angle is equal to the saturated optical tilt angle at a temperature close to T_{AC}. Upon entering the SmC^* from SmA^* phase, the azimuthal ordering

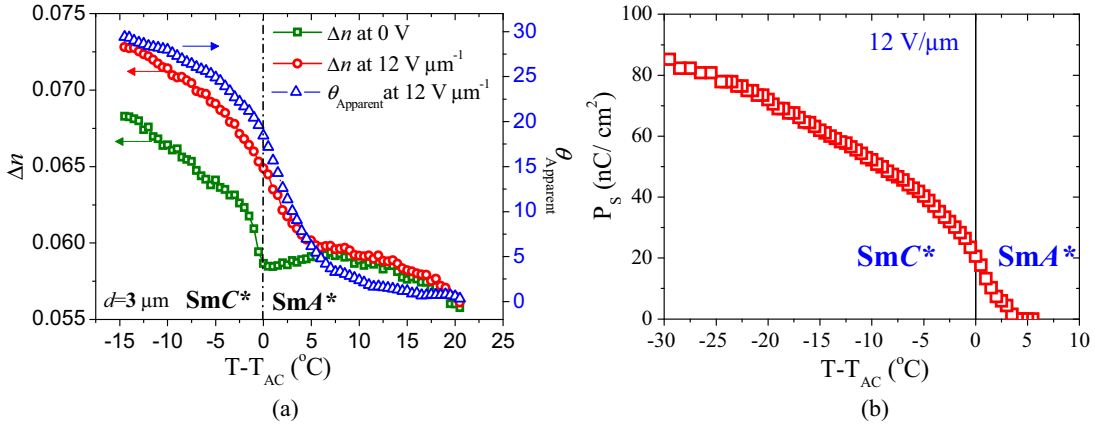

(a) (b)

FIG. 5. Results given here are for adpc042. (a) The temperature dependence of the apparent tilt angle (θ_{apparent}) and the birefringence Δn by applying a maximum field of 12 V μm^{-1} (red open circles); Δn in the absence of the electric field (green square). Blue triangles denote the apparent tilt angle θ_{apparent} for a field of 12 V/μm. Measurements are carried out on a 3 μm planar-aligned cell filled with adpc042 LC. (b) Spontaneous polarization P_S measured under the cooling process from the isotropic temperature plotted as a function of $(T-T_{\text{AC}})$. The measurements are carried out on a 5 μm planar-aligned cell by applying a square wave AC voltage of 12 ($V_{0-\text{peak}}/\mu$m) at a frequency of 110 Hz.

of the molecular directors on the cone localizes these onto a single orientation. In this case, the layer contraction is absent and then $d_C/d_{AC} \approx 1$, and therefore $R \approx 0$. Li *et al.* suggested another method of characterizing the de Vries quality from measurements of the layer thickness from XRD in terms of the de Vries coefficient, C_{deVries} [22]. The magnitude of this varies from "0" (classic rigid rod model with a maximum layer shrinkage) to 1 (ideal de Vries SmA^*- SmC^* transition with zero-layer shrinkage) such that

$$C_{\text{deVries}} = 1 - \left[\frac{(d_{AC} - d_C)}{(d_{AC}(1 - \cos\theta))}\right]. \quad (2)$$

The material adpc042 gives rise to $R \approx 0.373$ at 13 °C below the SmA^*-SmC^* transition temperature. Understandably, R is greater than zero but still low, hence the material is close to being a "de Vries smectic." An estimated value of C_{deVries} is ~0.86 (Fig. 4(a), inset) at 13 °C below the SmA^*-SmC^* transition temperature. The inset in Fig. 4(a) shows that both R and C_{deVries} are almost independent of temperature throughout the entire temperature range of the SmC^* phase. The lowest reported value of R so far in the literature is 0.17 for the chiral de Vries compound QL32-6, which exhibits a maximum layer contraction of only 0.2% at 3 °C below the SmA^*- SmC^* transitions with an optical tilt angle of 20° [13].

C. Electro-optical studies

The birefringence Δn and the apparent optical tilt angle θ_{apparent} are determined by recording the intensity of a transmitted beam of light through a LC cell by varying the positions of the polarizer and the analyzer. The procedure involves first keeping **P** fixed and then rotating the analyzer automatically by various angles. This procedure is repeated for at least three different positions of the polarizer. From the data, Δn and θ_{apparent} are calculated. This procedure is different from that given by Park *et al.* [23], who recorded the transmitted intensity by rotating the sample and also recorded the transmitted intensity for the **P** and **A** (i) parallel and (ii) perpendicular to each other. The experiment is conducted by applying a triangular signal of frequency 46 Hz and an amplitude of 12 $V_{0-\text{peak}}\mu\text{m}^{-1}$. The frequency of the field is chosen so as to allow sufficient time for the electro-optic switching to occur but to prevent ionic conductivity contributing to the switching current. An amplitude of the voltage applied to the LC sample adpc042 is large enough so as to make the tilt angle increase slowly with field and then eventually this is saturated by the field while avoiding the risk of damage to the sample by the applied electric field.

Figure 5(a) shows the results of the birefringence (Δn) as a function of temperature with and without electric field applied across the cell. Upon cooling the sample in the absence of a field from the isotropic to SmA^* phase, the magnitude of Δn first increases slightly but then starts to decrease within the SmA^* phase itself. This decrease in Δn with temperature is due to the de Vries tilt appearing in the SmA^* phase and a distribution of the in-layer directors occurring on the cone. Upon further cooling the sample in the absence of an electric field, Δn suddenly increases at the SmA^*-SmC^* phase-transition temperature T_{AC} followed by a slow increase with a decrease in temperature. An application of the electric field ($\boldsymbol{E} = 12\ \text{V}\ \mu\text{m}^{-1}$) gives rise to a continuous rise in Δn in the entire temperature range of the SmA^* and SmC^* phases. This field-induced increase in Δn is consistent with a change in the interference colors observed by POM (Fig. 3). The behavior is typical of the diffuse-cone model of the SmA^* phase with a weak first-order SmA^*- SmC^* phase transition [Fig. 2(d)]. In the conventional SmA^* of a LC, one expects only a very small increase in Δn to occur at the phase transition from a uniaxial SmA^* (with almost zero tilt angle at $T = T_{AC}$) to a biaxial SmC^* phase.

For adpc042, the measured value of the spontaneous polarization $\boldsymbol{P}_S$ [24] is plotted as a function of the reduced temperature in Fig. 5(b). Measurements are carried out on a 5 μm planar-aligned cell under the application of a square wave, frequency 110 Hz, and a large enough amplitude of 12 V/μm so as to saturate the induced polarization. The field is such that the helical structure for temperatures within SmC^* is fully unwound. It is interesting to note that the field-induced polarization in SmA^* phase is much higher than for conventional ferroelectric liquid crystals. $\boldsymbol{P}_S$ increases with a reduction in temperature below the SmA^*- SmC^* transition. The liquid-crystalline material under study yields $\boldsymbol{P}_S \sim 82.5\ \text{nC cm}^{-2}$ for $T = (T_{AC} - 30)\ ^\circ\text{C}$.

The measured values of θ_{apparent} as a function of the electric field for different temperatures in the SmA^* phase are plotted in Fig. 6(a). The coordinate system and the definition of the various angles are given in the electro-optical set-up shown in Fig. 6(b). At higher temperatures in the SmA^* phase, the magnitude of θ_{apparent} is small and it increases linearly with the applied field. For temperatures closer to T_{AC}, θ_{apparent} becomes nonlinear and continues to increase slowly up to an increasing electric field of 12 V μm^{-1}, and eventually the tilt angle tends to saturate with the electric field.

Several approaches exist in the literature for modeling the unusual electro-optic characteristics of the de Vries smectics [25–30]. The Langevin-Debye model, proposed by Fukuda [25] in a different context, was used by Clark *et al.* [27] to explain the electro-optical properties of de Vries smectic LCs. This model assumes that for a fixed temperature and zero electric field, the molecular directors in the SmA^* phase are tilted but azimuthally distributed onto a cone. In this model, the free energy is expressed as $U = -pE\cos\varphi$, where p is the local dipole moment. However, this model does not correctly explain the dependence of the induced apparent tilt angle (θ_{apparent} for the electric field) for temperatures rather closer to the SmA^*- SmC^* transition temperature T_{AC}. In 2013, the Boulder group [28] modified this model by adding an additional term involving the square of the electric field in the expression for the free energy. This is expressed as $U = -p_0 E\sin\theta\cos\varphi(1 + \alpha E\cos\varphi)$. Here, α is the phenomenological scaling factor and $p_0\sin\theta$ is the dipole moment of the domain correlated in the molecular tilt created by the condensation of azimuthal angles φ. The first term $-p_0 E\sin\theta\cos\varphi$ corresponds to the interaction of the dipole with the field. The second term $-\alpha p_0 E^2\sin\theta\cos^2\varphi$ includes the tilt susceptibility that increases with the square of the field E and it leads to a sigmoidal response in both Δn and θ_{apparent} with E. In this model, the field-induced θ_{apparent} varies between the values inferred from the Δn at zero field (θ_{min}) to the maximum electric field

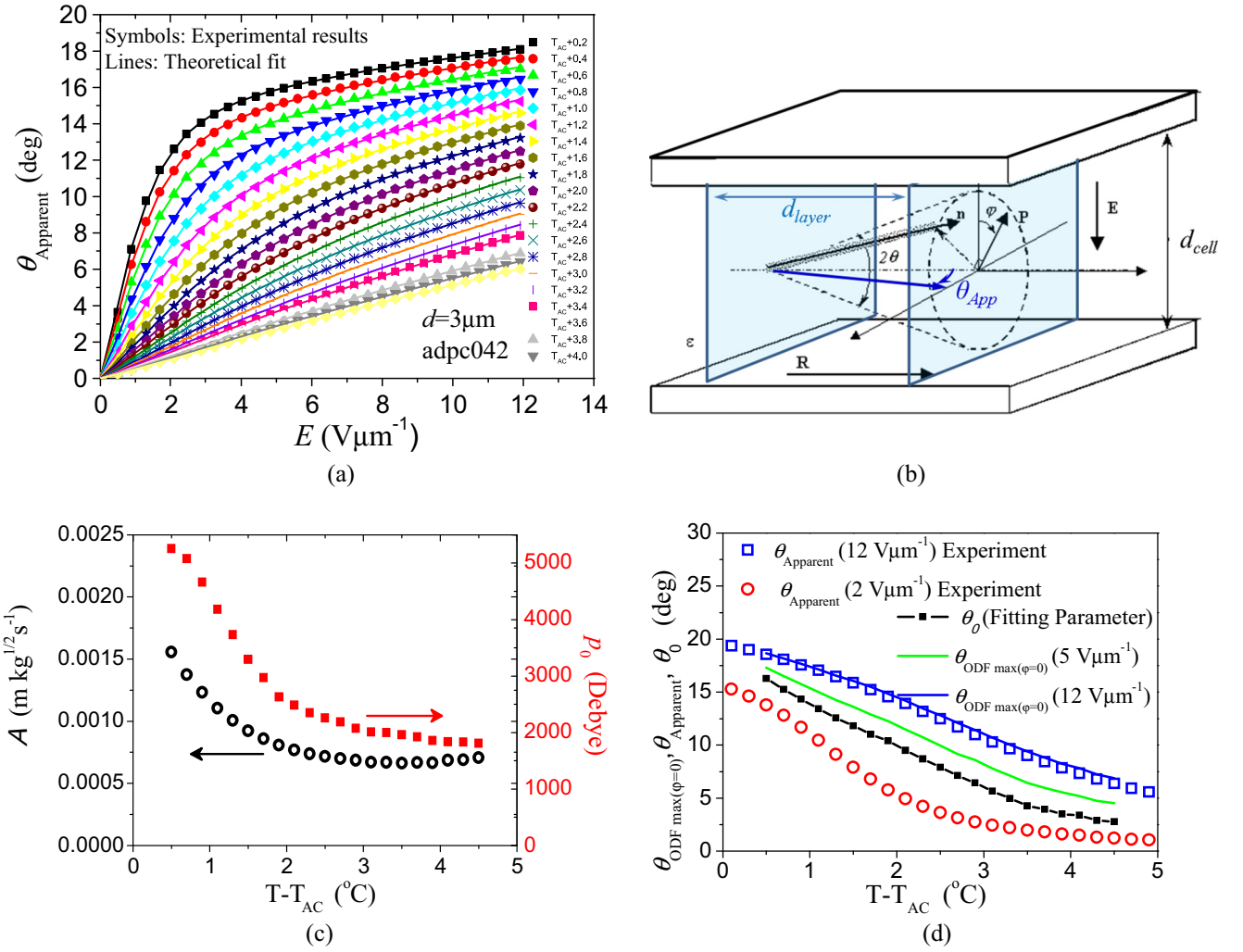

FIG. 6. (a) Variation of the field-induced apparent optical tilt θ_{apparent} (symbols) and the corresponding fitted values (solid lines) for selected temperatures. Measurements are carried out in a 3 μm planar-aligned cell filled with adpc042 LC. (b) The schematic of the dynamics for electro-optic set-up with the laboratory coordinate system. (c) Temperature dependence of the model parameters A and p_0 found from the experiments. (d) Temperature dependences of the measured apparent tilt angle θ_{apparent} (open symbols) and the cone angle θ_0 (the line with symbols) at positions of the distribution function of the maxima (lines) for the various electric-field strengths applied across a planar-aligned cell.

($\theta_{\max}$). These limiting values of $\theta_{\min}$ and $\theta_{\max}$ themselves are temperature-independent, but the actual values within these limits nevertheless are temperature-dependent. Therefore, we propose a somewhat different model. This involves three parameters (p_0, A and θ_0) for explaining the electro-optic response, where the mean-field free energy is expressed as

$$U = -p_0 E \sin\theta \cos\varphi + A^2 \sin^2(\theta - \theta_0). \tag{3}$$

Here the first term, $p_0 E \sin\theta\cos\varphi = \boldsymbol{P}\cdot\boldsymbol{E}$, describes the usual dipole interaction energy with the field. $|\boldsymbol{P}|$ $[= (p_0 \sin\theta)]$ is the magnitude of the dipole moment of a tilt-correlated domain. This first term of Eq. (3) is linear in the external electric field $\boldsymbol{E}$. The second term in this equation defines the cone distribution with a cone aperture angle of $2\theta_0$ and a distribution width proportional to $\sqrt{k_B T}/A$. Here k_B is the Boltzmann constant, T is the absolute temperature, and A is the phenomenological coefficient for the zero-field molecular distribution. Note that for the case $\theta_0 < \sqrt{k_B T}/A$, the model produces "sugarloaf" ODF [Fig. 7(a)], while a larger θ_0 combined with a narrower distribution width correspond to the "volcano" or "diffuse-cone" distribution [Fig. 7(a)]. Thus, both scenarios discussed in [29] are reproduced with the same expression for the free energy. Figure 7(b) illustrates the trend of $[(k_B T/A)^{1/2} - \theta_0]$ as a function of the reduced temperature $(T - T_{\text{AC}})$ for adpc042. One can see that at approximately 3° above the phase transition, this function crosses zero. This is a crossover between the sugarloaf and the diffuse-cone ODFs.

For the range of the electric fields used, we observe no inflection point in the field dependence of θ_{apparent}, i.e., no change in the slope of the derivative of the angle at the point. Therefore, we can achieve a good fit of the experimental data to the model without using terms of higher powers in E.

To simulate the behavior of θ_{apparent}, we use the mean-field approach combined with equations for the optical response [28]. An average $\langle Y\rangle$ over the orientational distribution can be written as $\langle Y\rangle = \int_0^{2\pi}\int_0^{\pi/2} Y(\theta,\varphi) f(\theta,\varphi)\sin\theta\, d\theta\, d\varphi$, where

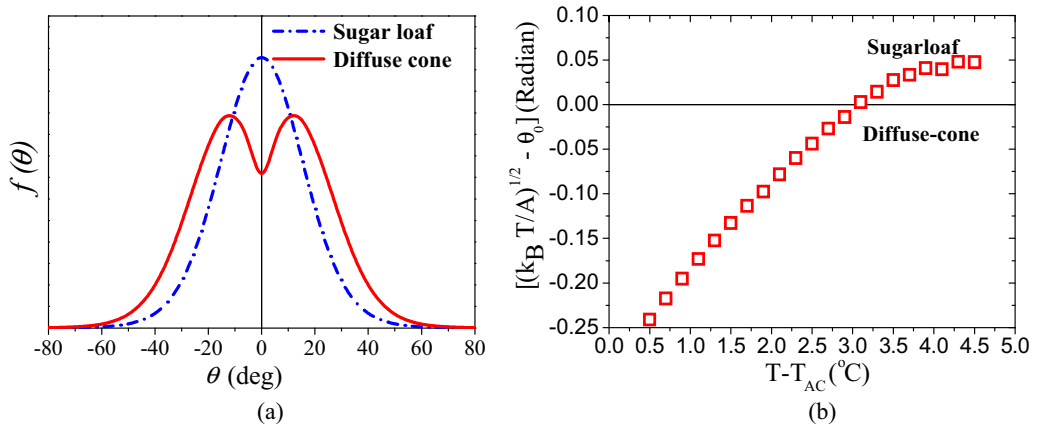

FIG. 7. (a) 2D schematic representation of sugarloaf (blue dash-dot lines) and diffuse-cone (red solid lines) (also called volcano-shaped) ODFs. (b) $[(k_BT/A)^{1/2} - \theta_0]$ plotted as a function of the reduced temperature $(T - T_{AC})$. Measurements are carried out on a 3 μm planar-aligned cell filled with adpc042.

the mean-field ODF $f(\theta, \varphi)$ is expressed as

$$f(\theta,\varphi) = \exp[-U/k_BT] \Big/ \int_0^{2\pi}\int_0^{\pi/2} \exp[-U/k_BT] \times \sin\theta\, d\theta\, d\varphi. \quad (4)$$

The apparent electro-optical tilt angle θ_{apparent} is given by

$$\tan 2\theta_{\text{apparent}} = \frac{\langle \sin 2\theta \cos\varphi\rangle}{\langle \cos^2\theta - \sin^2\theta\cos^2\varphi\rangle}. \quad (5)$$

Upon fitting the experimentally obtained voltage dependences of θ_{apparent} to the above model, we obtain values of p_0, A, and θ_0 each as a function of temperature [Figs. 6(c) and 6(d)]. All the parameters tend to increase upon approaching T_{AC} as the cell is cooled from the isotropic state to the SmA^* phase. Such an increase is in agreement with the previous models [27,28].

Upon using the dipole moment of the correlated domain as $p_0 \approx 5000$ D at 0.5 °C above the SmC^*-SmA^* phase-transition temperature, we can estimate the effective size of a domain using a procedure similar to that adopted by Shen *et al.* [28]. The effective molecular dipole moment can be estimated from the polarization density measurements performed on a planar-aligned cell in the SmC^* phase. In this case, P_S is saturated at 69 nC/cm^2; $\theta_{\text{apparent}} = 30^\circ$ at $(T_{AC} - 19)$ °C, with the molar mass $M = 590.3$ g/mol, density $\rho = 1.2$ g/cm^3, and the dipole moment is found as $\mu_{\text{eff}} = \frac{P_S M}{\rho N_A \sin\theta_{\text{apparent}}} \approx 0.34$ D. Therefore, the tilt-correlated domain in our experiment contains approximately 6000–15 000 molecules. The effective domain correlation length $\sqrt[3]{\frac{p_0 \sin\theta_{\text{apparent}}}{P_S}}$, at a temperature close to the SmA^*-SmC^* phase transition, is of the order of 30 nm [30].

Parameter A clearly favors the "volcano"-type distribution as illustrated by Fig. 8. A comparison of the cone angle θ_0 that fits the experimentally obtained θ_{apparent} for different fields is shown in Fig. 6(d). Note that for higher field strengths, θ_{apparent} exceeds θ_0. This is indicative of a large electroclinic effect. The solid lines in Fig. 6(d) show angular positions of the maximum in the ODF simulated for the two electric-field strengths (5 and 12 V μm^{-1}) here. The experimental values of θ_{apparent} for 12 V μm^{-1} are slightly lower than for an angle for which θ_{ODF} is a maximum. This is expected from a highly distorted difuse-cone ODF; the distortion is brought about by the applied electric field.

Figures 8(a)–8(c) show a 3D illustration of the ODF function obtained for a temperature of $(T_{AC} + 1)$ °C in the SmA^* phase. The ODF is normalized as given below such that its volume for different fields is a constant: $f_{3D} = \frac{f(\theta,\varphi)}{\sqrt[3]{\int_0^{2\pi}\int_0^{\pi/2} f(\theta,\varphi)^3 \sin\theta d\theta d\varphi}}$. Figure 8(c) shows the cross section of the ODF in the plane of the LC cell where the maximum of the

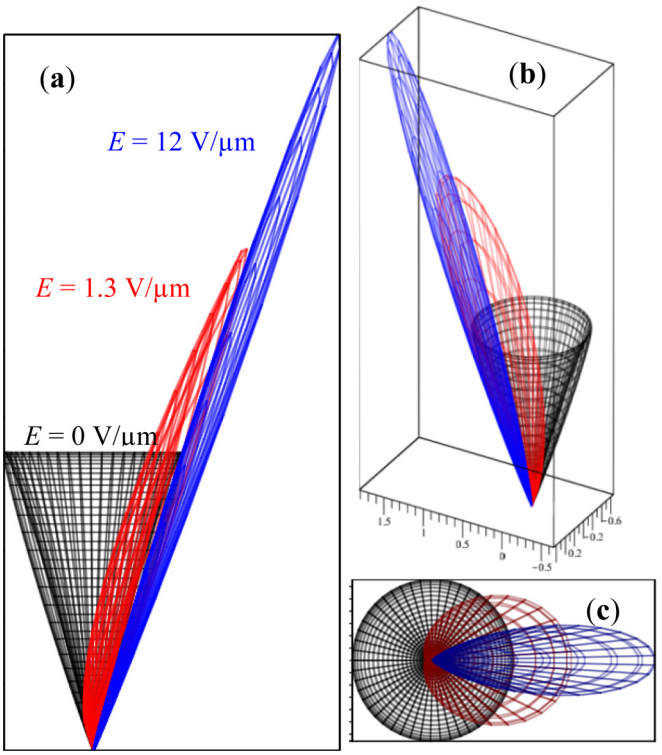

FIG. 8. The ODF of the smectic compound, adpc042, at a temperature of $T = (T_{AC} + 1)$ °C for different electric field strengths (0 V, 1.3 V μm^{-1}, and 12 V μm^{-1}). Parts (a)–(c) are the axonometric projections of $f_{3D}(\theta, \varphi)$.

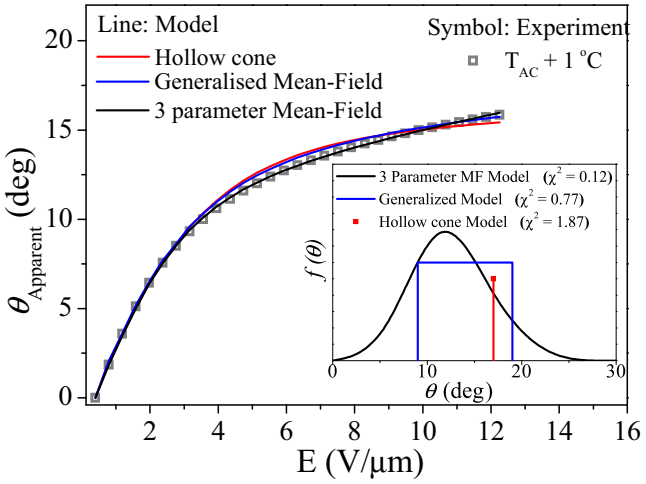

FIG. 9. The experimental θ_{apparent} (□) vs electric field E shown at a temperature of 1 °C above the SmA^*- SmC^* phase-transition temperature, T_{AC}, is fitted to various models: The hollow cone, the generalized mean field (MF), and the three-parameter MF one. A schematic representation of the ODFs for the three models under discussion is given in the inset.

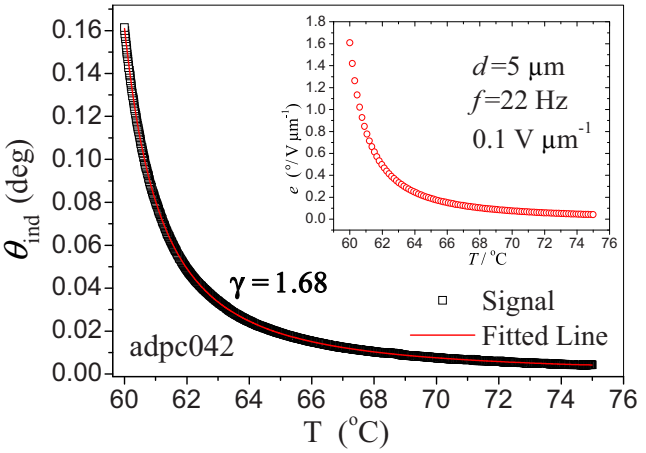

FIG. 10. The temperature dependence of electroclinic response θ_{ind} of adpc042 (□): experimental value; red line (—): fitting to Eq. (7). The inset is the electroclinic coefficient e (red open circle) calculated using the equation $e = \theta_{\text{ind}}/E$ as a function of temperature. Experiments were conducted under cooling within the temperature range of SmA^* phase down to a temperature of $T = (T_{\text{AC}} + 1)$ °C by the application of 0.1 $V_{0-\text{peak}}\mu\text{m}^{-1}$ (planar-aligned cell, $d = 5\ \mu$m sine wave ac voltage of 22 Hz).

ODF versus the apparent tilt angle is plotted. The electroclinic effects for the following electric fields are given in Fig. 8: zero, moderate (1.3 V/μm) ("cone unwinding"), and for large fields, 12 V/μm (tilt increases but φ is condensed within a narrow range of values). Note that the modeled ODF shown in Fig. 8 corresponds to the core part of the mesogen that exhibits birefringence at visible wavelengths of light.

To test different models, we fit experimental data of θ_{apparent} as a function of the electric field at a temperature 1 °C above the SmC^*- SmA^* phase-transition temperature, T_{AC} (Fig. 9), to the following models: the fixed-angle hollow cone [27], the generalized mean-field model [28], and our three-parameter mean-field model. For low fields, data fitted to the various models are quite adequate. However, for medium and high electric fields, the three-parameter model shows a closer fit to the experimental data. This is supported by drawing a comparison between the sum of the squares of the residuals (χ^2) for the various fits as shown in the inset of Fig. 9. Though the three models provide a reasonable fit to the data, our proposed model has no intrinsic assumption of either the sugarloaf or the diffuse cone-type (volcano) distribution, i.e., it is not limited to the assumption of a certain ODF in the SmA^* phase. Therefore, testing and discrimination among the models are carried out automatically during the fitting procedure. Moreover, the model produces a continuous function for the ODF, having a better physical significance.

The de Vries LCs normally exhibit large values of the electroclinic coefficient (denoted by e) [19,32,33]. The electroclinic response is recorded for the material adpc042 in a planar-aligned cell. The experiment is carried out by keeping the smectic layer normal at an angle of 22.5° with respect to the polarizer. The light intensity I, transmitted through the LC cell, in the absence of the field $\boldsymbol{E}$ is given by

$$I = I_0 \sin^2(2\alpha)\sin^2(\pi \Delta n d/\lambda), \tag{6}$$

where I_0 is the incident intensity, α is the angle between the molecular director and the polarizer, Δn is the birefringence, d is the cell thickness, and λ is the wavelength of the incident light. When an electric field is applied across the cell, the transmitted intensity varies linearly with the induced tilt angle $\delta\alpha = \theta_{\text{ind}}$. Differentiating Eq. (6) with respect to α is given as

$$\delta I = 2I_0 \sin(4\alpha)\sin^2(\pi \Delta n d/\lambda)\theta_{\text{ind}}. \tag{7}$$

From Eqs. (6) and (7) and for $\alpha = 22.5°$ we obtain $\theta_{\text{ind}} = \delta I/4I$. Figure 10 shows θ_{ind} as a function of temperature over the temperature range of the SmA^* phase. The magnitude of θ_{ind} increases with decreasing temperature. Upon approaching T_{AC} from the high-temperature side of SmA^*, the magnitude of θ_{ind} diverges, and this corresponds to the divergence of the correlation length of the tilt domain; here the azimuthal angle is condensed to lie within narrower limits.

The amplitude of θ_{ind} with temperature can be expressed by the power-law equation as follows [34]:

$$\theta_{\text{ind}} = \frac{C}{(T - T_{\text{AC}})^{\gamma}}. \tag{8}$$

Here C is the scaling constant, T_{AC} is the SmA^*- SmC^* transition temperature, and γ is the critical exponent. For the smectic material under investigation, $\gamma = 1.68$. For a conventional SmA^*- SmC^* transition, γ is 1.33 [35]. Values of γ greater than 1.33 reflect the short-range correlation of molecular directors in three dimensions, again a characteristic of the de Vries smectics. The inset in Fig. 10 shows the temperature dependence of the electroclinic coefficient e, calculated from the definition of $e = \theta_{\text{ind}}/E$.

D. Dielectric spectroscopy

Figure 11(a) shows a three-dimensional plot of temperature-dependent dielectric loss spectra (ε'') of a

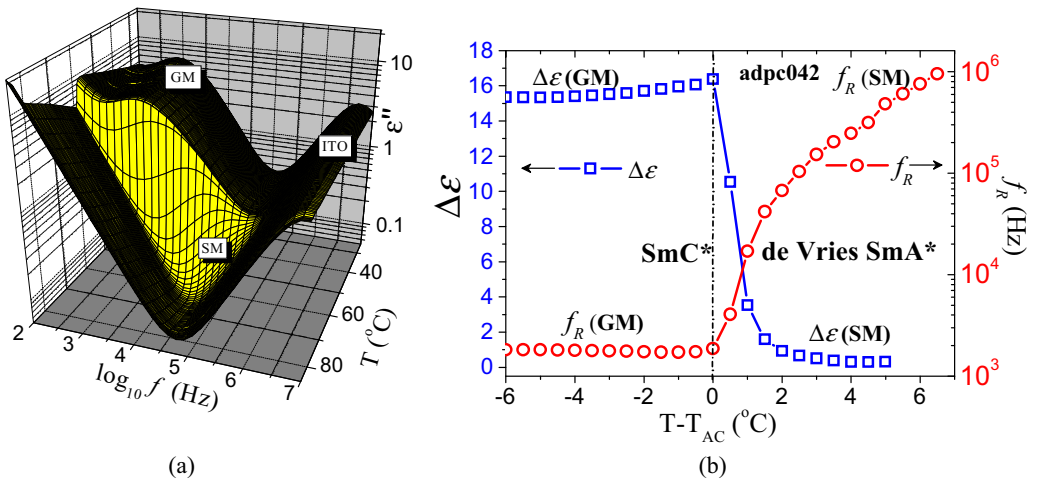

(a) (b)

FIG. 11. (a) A 3D plot of temperature-dependent dielectric loss spectra (ε'') of the compound adpc042 (cell thickness, $d = 10\,\mu$m) in a planar-aligned cell. The dielectric measurements are carried out under cooling. Temperature stabilization is 0.05 °C and the applied voltage is 0.1 $V_{\rm rms}$. (b) Dielectric strength $\Delta\varepsilon$ (open blue squares) and the corresponding relaxation frequency f_R (red open circles) are plotted as a function of temperature. SM and GM refer to the soft and Goldstone modes, respectively.

planar-aligned cell filled with the material adpc042 LC. Note that the temperature-independent high-frequency process is due to the resistance of ITO in series with the capacitance of the filled cell. The relaxation process in the SmA^* phase corresponds to the fluctuations of the tilt angle, and the mode due to tilt angle fluctuations is known as the soft mode (SM). This arises mainly as the system approaches $T_{\rm AC}$ and the elastic constant controlling the tilt fluctuations decreases or gets softer. The low-frequency dielectric relaxations in the SmC^* phase are associated with the Goldstone (GM) mode, in which the molecular director is subjected to continual symmetry breaking.

The dielectric spectra are analyzed using the Novocontrol WINFIT program. The temperature-dependent dielectric strength $\Delta\varepsilon$ and the relaxation frequency f_R are obtained by fitting the dielectric spectra to the Havriliak-Negami equation [36]:

$$\varepsilon^*(\omega) = \varepsilon' - i\varepsilon'' = \varepsilon_\infty + \sum_{j=1}^{n} \frac{\Delta\varepsilon_j}{[1+(i\omega\tau_j)^{\alpha_j}]^{\beta_j}} - \frac{i\sigma_{\rm dc}}{\varepsilon_0\omega}, \quad (9)$$

where ε_∞ is the high-frequency permittivity depending on the electronic and atomic polarizability, j is the number of relaxation processes, which varies from 1 to n, $\omega = 2\pi f$ is the angular frequency in radians, ε_0 is the free-space permittivity, τ_j is the relaxation time of the jth process, $\Delta\varepsilon_j$ is the dielectric strength, and α_j and β_j are the symmetric and asymmetric broadening parameters of the jth dielectric relaxation process related to the distribution of relaxation times. The term $(-i\sigma_{\rm dc}/\varepsilon_0\omega)$ gives the dielectric loss due to the ionic conduction, and it is dominant at lower frequencies due to the inverse ω term. The relaxation frequency f_j of the jth process is related to τ_j as [37]

$$f_j = \frac{1}{2\pi\tau_j}\left[\sin\left(\frac{\alpha_j\pi}{2+2\beta_j}\right)\right]^{1/\alpha_j}\left[\sin\left(\frac{\alpha_j\beta_j\pi}{2+2\beta_j}\right)\right]^{-1/\alpha_j}. \quad (10)$$

The temperature dependencies of $\Delta\varepsilon$ and f_R are shown in Fig. 11(b). The amplitude of $\Delta\varepsilon$ shows a pronounced increase when the system approaches $T_{\rm AC}$ from the SmA^* phase. The maximum value of $\Delta\varepsilon$ at $T_{\rm AC}$ is 16.8. The corresponding f_R is decreasing in the SmA^* phase with a sharper trend in its lower-temperature range. Remarkably strong soft-mode dielectric absorption is observed in the dielectric spectra of de Vries LCs [38–40] in contrast to the compounds that exhibit a conventional SmA^* [41]. The observation of a large pyroelectric current observed in a siloxane based chiral polymer can now be explained in terms of de Vries characteristics [42].

IV. CONCLUSION

We have designed and synthesized two 5-phenyl pyrimidine derivatives with siloxane and also with fluorocarbon chain terminations, both with a chiral (R, R)-2,3-epoxyhexoxy side chain. Mesophases formed by these compounds are investigated using a number of techniques, including DSC, POM, XRD, birefringence, electro-optical, and dielectric spectroscopy.

We find that the maximum layer contraction for the siloxane-terminated adpc042 at a temperature of 13 °C below the SmA^*-SmC^* transition is 1.7%, and a reduction factor R is 0.37 on a scale of 1 to 0. This compound is considered to be a good "de Vries smectic" with the de Vries coefficient $C_{\rm deVries}$ of 0.86 on the scale of 0 to 1. The soft-mode dielectric relaxation strength $\Delta\varepsilon$ shows a critical behavior when the system approaches the SmA^*-SmC^* transition from the high-temperature side. The critical exponent of the electroclinic response is found to be $\gamma = 1.68$. The value of the exponent is much greater than 1.33, found for most conventional smectics. The temperature dependence of the correlation length suggests that the material has de Vries characteristics.

We introduce a three-parameter MF model for describing the ODF of the molecular director in the SmA^* phase with a view toward fitting the field-induced experimental apparent tilt angle $\theta_{\rm apparent}$ data as a function of the electric field. Close

to the SmA^*- SmC^* transition temperature, the birefringence in the SmA^* phase is seen to decrease with a reduction in temperature. This is due to the emergence of a nonzero value of cone angle θ, the magnitude of which increases to 17° as the SmA^*- SmC^* phase transition is approached. The proposed model fits the experimental data on apparent tilt angle and leads to the diffuse-cone ODF, at temperatures close to the phase-transition temperatures. However, θ_0 decreases with an increase in temperature, and the ODF displays a crossover from the diffuse cone to the sugarloaf at ∼3.1 °C above T_{AC}.

ACKNOWLEDGMENTS

Work was supported by 13/US/I2866 from the Science Foundation Ireland as part of the U.S.-Ireland Research and Development Partnership program jointly administered with the U.S. National Science Foundation under Grant No. NSF-DMR-1410649. Financial support for the Belfast group was from the Department for Employment and Learning under grant code USI 056. X-ray measurements were done in Warsawa, under the EU Cost ICI 1208 2014–17 project. We thank Satyendra Kumar for coordinating the U.S.-Ireland project.

APPENDIX: SYNTHETIC PROCEDURE

All reagents were purchased from Sigma Aldrich, Fluorochem, Alfa Aesar, ABCR, Synthonix and used without any further purification. Solvents were purchased from Sigma Aldrich. DMF was purchased pre-dried, THF was dried using a sodium/benzophenone still under N_2, and DCM was dried using CaH_2. All reactions were generally carried out under argon using oven-dried glassware. TLC plates were performed on Merck silica gel 60 F_{254} and were visualized using a light source with a wavelength of 254-nm. Flash column chromatography was performed on Fluorochem silica gel 60 (40–63 μm).

Infrared (IR) spectra were recorded using a Perkin-Elmer Spectrum Two FTIR spectrometer. ^{1}H and ^{13}C spectra were recorded at 25 °C ($CDCl_3$ as solvent and TMS as reference) using a Bruker 400 MHz Ultrashield (Avance 400). HRMS spectra were recorded using a Waters-TOF Electrospray micromass LCT premier. Optical rotations were recorded using a polarimeter Perkin-Elmer: model 341 Polarimeter.

The synthesis of adpc042 was carried out through the scheme shown in Fig. 12.

Further details of the synthesis and characterization of each stage of intermediates are given below:

The chemical structure of compound 1 is given in Fig. 13.

5-Hexen-1-ol (0.62 g, 6.2 mmol) was dissolved in dry toluene (15 mL) and sealed in a Schlenk under argon. Sodium (0.16 g, 7.00 mmol) was added as a solid, and the solution was stirred at 50 °C overnight. 5-Bromo-2-chloropyrimidine (1.00 g, 5.17 mmol) was added, and the solution stirred for 8 h at 50 °C. The solution was filtered, water (20 mL) was added, and the crude extracted with ethyl acetate (3 × 30 mL). The product was purified by column chromatography (ethyl acetate: hexane, 1:9, $R_f = 0.45$) to yield a colorless oil (0.80 g, 3.11 mmol, 60%).

^{1}H NMR (400 MHz, $CDCl_3$) δ: 8.51 (s, 2H), 5.81 (ddt, J = 6.67, 6.67, 10.18, 16.91, H), 4.98 (m, 2H), 4.33 (t, J = 6.60, 2H), 2.12 (m, 2H), 1.82 (m, 2H), 1.57 (m, 2H).

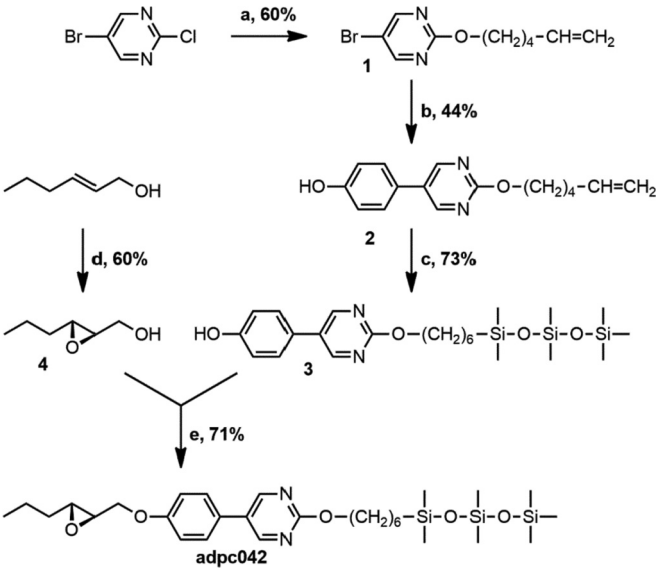

FIG. 12. General scheme for the preparation of adpc042. **a:** 5-hexenol, Na, 50° C overnight, toluene. **b:** 4-hydroxyphenylboronic acid, K_2CO_3, $Pd(Ph_3P)_4$, MeOH/toluene 100° C overnight. **c:** 1,1,1,3,3,5,5heptamethyltrisiloxane, platinum(0)-1,3-divinyl-1,1,3,3-trimethyldisiloxane, THF, 2h 25° C. **d:** Shi catalyst, Bu_4NHSO_3, CH_3CN, AcOH, 3h 0° C. **e:** Ph_3P, DEAD, THF, 12h, 25° C.

^{13}C NMR (101 MHz, $CDCl_3$) δ: 164.15 (C), 159.75 (2CH), 138.59 (CH), 115.01 (CH_2), 111.79 (C), 68.42 (CH_2), 33.55 (CH_2), 28.36 (CH_2), 25.36 (CH_2).

IR (film): $\tilde{\nu}$ = 3076, 2936, 1640, 1570, 1432, 1332, 1176, 1122, 1024, 912, and 794 cm^{-1}.

HRMS (EI): m/z calculated for $C_{20}H_{27}N_4O_2Br_2[2M + H^+]$ 513.0501, found: 513.0513.

The chemical structure of compound **2** in Fig. 12 is given in Fig. 14 and the synthesis and characterization are detailed below:

4-hydroxyphenylboronic acid (0.32 g, 2.33 mmol) and **1** (0.50 g, 1.94 mmol) were sealed in a Schlenk under argon. Toluene (12 mL) was added and the solution degassed for 5 min. Degassed methanol (7 mL) and potassium carbonate dissolved in degassed water (3 mL) were added to the Schlenk. Tetrakis(triphenylphosphine)palladium(0) (0.11 g, 0.10 mmol) was added as a solid, and the solution was refluxed overnight. The crude was concentrated, and water (30 mL) was added before extraction with DCM (3 × 30 mL). The organic phase was dried with magnesium sulfate and concentrated *in vacuo*. The product was purified by column chromatography (ethyl acetate: DCM, 15:85, where $R_f = 0.57$ in ethyl acetate: hexane, 1:1) to yield a white solid (0.23 g, 0.85 mmol, 44%).

^{1}H NMR (400 MHz, $CDCl_3$) δ: 8.66 (s, 2H), 7.90 (s, 1H), 7.37 (d, J = 8.72, 2H), 7.03 (d, J = 8.71), 5.79 (ddt, J =

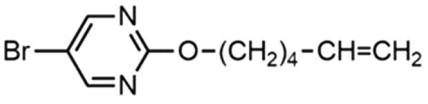

FIG. 13. Chemical structure of compound **1**.

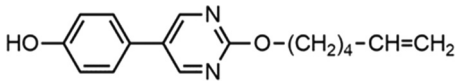

FIG. 14. Chemical structure of compound **2** in Fig. 12.

6.65, 6.65, 10.18, 16.91, 1H), 4.97 (m, 2H), 4.42 (t, $J = 6.58$, 2H), 2.11 (m, 2H), 1.85 (m, 2H), 1.58 (m, 2H).

^{13}C NMR (101 MHz, $CDCl_3$) δ: 164.22 (C), 157.17 (C), 156.95 (2CH), 138.61 (CH), 128.48 (C), 127.98 (2CH), 126.19 (C), 116.73 (2CH), 114.97 (CH_2), 68.06 (CH_2), 33.55 (CH_2), 28.48 (CH_2), 25.38 (CH_2).

IR (film): $\tilde{\nu} = 3099$, 3022, 2950, 1602, 1558, 1434, 1326, 1270, 1180, 1072, 924, and 834 cm^{-1}.

HRMS (EI): The molecular weight for $C_{16}H_{19}N_2O_2$ [M + H^+] was calculated as 271.1447 and found to be 271.1446.

The chemical structure of compound **3** is given in Fig. 15; synthesis and characterization are detailed below:

2 (0.22 g, 0.81 mmol) was dissolved in dry THF (12 mL) under argon. 1,1,1,3,3,5,5-heptamethyltrisiloxane (0.35 g, 1.59 mmol) and platinum(0)-1,3-divinyl-1,1,3,3-tetramethyldisiloxane (0.20 mL of 0.1 M solution, 0.02 mmol) were added to the flask, and the solution was stirred for 2 h. The crude is concentrated and purified by column chromatography (ethyl acetate: hexane, 2:8, where $R_f = 0.30$ in ethyl acetate: hexane, 3:7) to yield a colorless wax (0.29 g, 0.59 mmol, 73%).

^{1}H NMR (400 MHz, $CDCl_3$) δ: 8.65 (s, 2H), 7.39 (d, J = 8.70), 6.96 (d, $J = 8.72$, 2H), 5.37 (s, 1H), 4.39 (t, $J = 6.72$), 1.83 (m, 2H), 1.42 (m, 6H), 0.54 (m, 2H), 0.08 (s, 9H), 0.06 (s, 6H,), 0.02 (s, 6H).

^{13}C NMR (101 MHz, $CDCl_3$) δ: 164.71 (C), 157.08 (CH), 156.18 (C), 128.11 (CH), 128.08 (C) 127.30 (C), 116.48 (CH), 68.19 (CH_2), 33.36 (CH_2), 29.07 (CH_2), 25.91 (CH_2), 23.39 (CH_2), 18.47 (CH_2), 2.04 ($3CH_3$), 1.50 ($2CH_3$), 0.41 ($3CH_3$).

IR (film): $\tilde{\nu} = 2958$, 1600, 1442, 1332, 1258, 1048, and 840 cm^{-1}.

HRMS (EI): m/z calculated for $C_{23}H_{41}N_2O_4Si_3$ [M + H^+] 493.2374, found: 493.2379.

The chemical structure of compound 4 in Fig. 12 is given in Fig. 16, and other details are followed below:

Trans-2-hexen-1-ol (1.00 g, 9.98 mmol), Shi Epoxidation Diketal Catalyst (0.77 g, 3.00 mmol), and tetrabutylammonium hydrogensulfate (0.06 g, 0.18 mmol) were dissolved in dimethoxymethane/acetonitrile (100 mL, 2:1). Acetic acid (0.35 mL) was added to potassium carbonate (70 mL of 0.1 M solution), and this was added to the reaction, which was then cooled to −10 °C. Oxone (8.48 g, 13.78 mmol) was dissolved in ethylenediaminetetra-acetic acid disodium salt (50 mL of 0.004 M solution in water), and potassium carbonate (8.00 g, 57.91 mmol) was dissolved in water (50 mL). The oxone and the carbonate solution were added to the reaction flask dropwise over 3 h while keeping the temperature below 0 °C. Water was added, and the organic phase extracted with DCM (3 × 50 mL) before drying with magnesium sulfate and

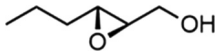

FIG. 16. Chemical structure of compound **4** in Fig. 12.

increasing the concentration of the solution. The epoxide was purified by column chromatography (hexane: diethyl ether, 2:1 → 100% ether once product appears, $R_f = 0.53$ in DCM: ethyl acetate, 1:1) to yield a colorless oil (0.70 g, 5.99 mmol, 60%). The column was compacted using hexane: diethyl ether, 2:1 and 1% triethylamine to neutralize the silica.

^{1}H NMR (400 MHz, $CDCl_3$) δ: 3.91 (ddd, $J = 2.58, 5.58$, 12.53, 1H), 3.63 (ddd, $J = 4.30$, 7.29, 12.52), 2.96 (td, J = 2.36, 5.50, 5.65, 1H), 2.92 (m, 1H), 1.74 (m), 1.50 (m, 3H), 0.96 (t, $J = 7.26$, 3H).

^{13}C NMR (101 MHz, $CDCl_3$) δ: 61.93 (CH_2, 58.55 (CH), 56.01 (CH), 33.78 (CH_2), 19.47 (CH_2), 14.10 (CH_3).

IR (film): $\tilde{\nu} = 3418$, 2962, 2874, 1650, 1464, 1382, 1220, 1046, 900, and 849 cm^{-1}.

$[\alpha]_D^{20}$: +38.75 (c 0.022, $CHCl_3$).

The chemical structure of adpc042 is given in Fig. 17 and other details are followed below:

3 (0.56 g, 1.14 mmol), **4** (0.12 g, 1.03 mmol), and triphenylphosphine (0.33 g, 1.26 mmol) were dissolved in dry THF (20 mL) under argon. Diethyl azodicarboxylate (0.22 g, 1.24 mmol) was dissolved in dry THF (8 mL) under argon before being added dropwise to the reaction flask. The flask was stirred overnight and then concentrated. The product was purified by column chromatography (ethyl acetate: hexane, 1:9, where $R_f = 0.60$ in ethyl acetate: hexane, 3:7) to yield a white wax (0.43 g, 0.73 mmol, 71%).

^{1}H NMR (400 MHz, $CDCl_3$) δ: 8.65 (s, 2H), 7.43 (d, J = 8.81, 2H), 7.02 (d, $J = 8.81$, 2H), 4.38 (t, $J = 6.71$, 2H), 4.23 (dd, $J = 3.34$, 11.08, 1H), 4.02 (dd, $J = 5.52$, 11.08), 3.13 (ddd, $J = 2.29$, 3.27, 5.53, 1H), 2.98 (td, $J = 2.20$, 5.53, 5.64, 1H), 1.83 (m, 2H), 1.65-1.30 (m, 10H), 0.99 (t, J = 7.28), 0.54 (m, 2H), 0.08 (s, 9H), 0.06 (s, 6H), 0.01 (s, 6H).

^{13}C NMR (101 MHz, $CDCl_3$) δ: 164.76 (C), 158.92 (C), 157.10 (2CH), 127.95 (C), 127.89 (2CH), 127.68 (C), 115.71 (2CH), 68.82 (CH_2), 68.15 (CH_2), 56.66 (CH), 56.22 (CH), 33.84 (CH_2), 33.36 (CH_2), 29.06 (CH_2), 25.91 (CH_2), 23.39 (CH_2), 19.44 (CH_2), 18.46 (CH_2), 14.10 (CH_3), 2.04 ($3CH_3$), 1.50 ($2CH_3$), 0.40 ($2(CH_3)$.

IR (film): $\tilde{\nu} = 2958$, 1598, 1548, 1448, 1256, 1048, and 840 cm^{-1}.

HRMS (EI): m/z calculated for $C_{29}H_{51}N_2O_5Si_3$ [M + H^+] 591.3096, found: 591.3097.

$[\alpha]_D^{20}$: +9.74 (c 0.029, $CHCl_3$).

The synthesis of DR257 was carried out through the scheme shown in Fig. 18; further details of each stage are provided below.

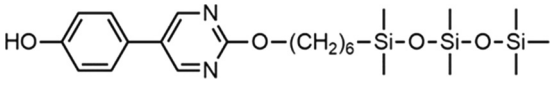

FIG. 15. Chemical structure of compound **3** in Fig. 12.

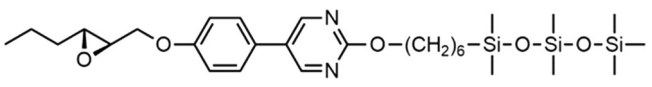

FIG. 17. Chemical structure of compound adpc042 in Fig. 12.

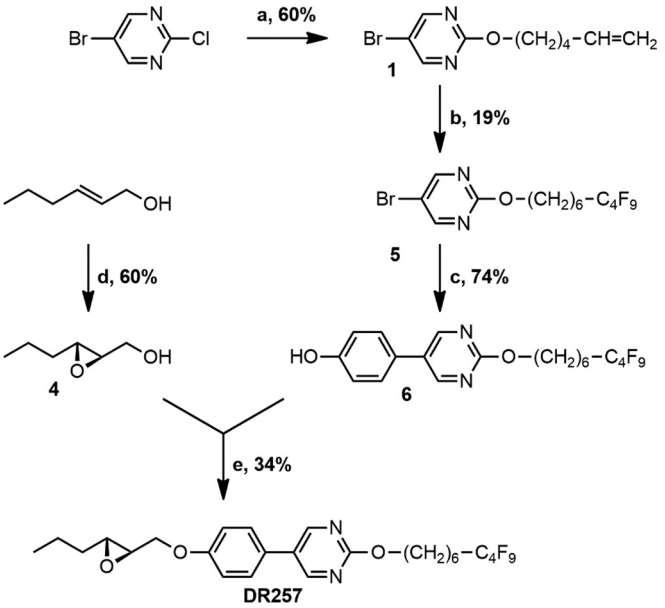

FIG. 18. General scheme for the preparation of DR257. **a:** 5-hexenol, Na, 50° C overnight, toluene. **b:** $Na_2S_2O_4$, Na_2HPO_4, 1-iodoperfluorobutane, CH_3CN/H_2O, 25° C, 12 hr. **c:** 4-hydroxyphenylboronic acid, K_2CO_3, $Pd(Ph_3P)_4$, MeOH/toluene 100° C 12h. **d:** Shi catalyst, Bu_4NHSO_3, CH_3CN, AcOH, 3h 0° C. **e:** Ph_3P, DEAD, THF, 12h, 25° C.

Synthesis and characterization of the intermediates are given below. The structure of the compound **5** is given in Fig. 19 and details follow below:

$Na_2S_2O_4$ (0.040 g, 0.230 mmol) and Na_2HPO_4 (0.039 g, 0.276 mmol) were added to a mixture of 1-iodoperfluorobutane (0.955 g, 2.76 mmol), the alkene **1** (0.590 g, 2.30 mmol) in H_2O/CH_3CN (12 mL 1:3) [43]. The mixture was stirred overnight at room temperature. Et_2O and H_2O were added to the mixture, and the phases were separated. The organic phase was extracted with Et_2O (2 × 10 mL) and the combined organic phase was dried with magnesium sulfate. The solvent was removed at reduced pressure to produce a yellow oil. This iodinated intermediate was used without further purification. Bu_3SnH (0.802 g, 2.76 mmol) and a catalytic amount of AIBN (12 mg) were added to the oil. The reaction mixture was heated to 110 °C for 24 h. The solvent was removed and the crude of reaction was purified by column chromatography on silica gel (hexane:ethyl acetate = 9 : 1) to give **5** (0.208 g, 19% yield).

^{1}H NMR (400 MHz, $CDCl_3$) δ: 8.51 (s, 2H), 4.33 (t, J = 6.5, 2H), 2.17–1.95 (m, 2H), 1.90–1.75 (m, 2H), 1.63 (m, 2H), 1.55–1.39 (m, 4H).

^{13}C NMR (101 MHz, $CDCl_3$) δ: 164.11 (C), 159.79 (2CH), 111.89 (C), 68.32 (CH_2), 31.15 (CH_2), 30.70 (t, J = 22.3, CH_2), 29.00 (CH_2), 28.69 (CH_2), 25.83 (CH_2), 20.29 (t, J = 3.7, CH_2).

^{19}F NMR (376 MHz, $CDCl_3$) δ: −81.07, −114.61, −124.51, −126.06.

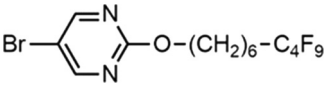

FIG. 19. Chemical structure of compound **5** in Fig. 18.

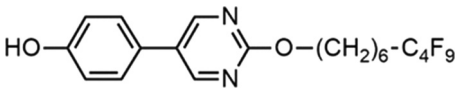

FIG. 20. Chemical structure of compound **6** in Fig. 18.

HRMS (EI): molecular weight calculated for $C_{14}H_{15}BrF_9N_2O[M + H^+]$ 477.0224; found as 477.0208.

The chemical structure of compound 6 is given in Fig. 20 and other details follow:

4-hydroxyphenylboronic acid (0.070 g, 0.501 mmol) and **5** (0.220 g, 0.462 mmol) were sealed in a Schlenk under argon. Toluene (12 mL) was added and the solution degassed for 5 min. Degassed methanol (4 mL) and potassium carbonate dissolved in degassed water (1 mL) were added to the Schlenk. Tetrakis(triphenylphosphine)palladium(0) (0.029 g, 0.025 mmol) was added as a solid, and the solution was refluxed overnight. The crude was concentrated, and water (10 mL) was added before extraction with DCM (3 × 10 mL). The organic phase was dried with magnesium sulfate and concentrated *in vacuo*. The product was purified by column chromatography (ethyl acetate:hexane, 3:7, where $R_f = 0.35$ in ethyl acetate: hexane, 3:7) to yield a white solid (0.169 g, 0.345 mmol, 75%).

^{1}H NMR (400 MHz, $CDCl_3$) δ: 8.65 (s, 2H), 7.39 (d, J = 8.6, 2H), 6.96 (d, J = 8.5, 2H), 5.58 (s, 1H), 4.39 (m, 2H), 2.07 (m, 2H), 1.86 (m, 2H), 1.65 (m, 2H), 1.57–1.42 (m, 4H).

^{13}C NMR (101 MHz, $CDCl_3$) δ: 164.56 (C), 157.09 (2CH), 156.32 (C), 128.25 (C), 128.09 (2CH), 127.09 (C), 116.51 (2CH), 67.79 (CH_2), 30.94 (t, J = 22.3, CH_2), 29.05 (CH_2), 28.86 (CH_2), 25.90 (CH_2), 20.28 (t, J = 3.7, CH_2).

^{19}F NMR (376 MHz, $CDCl_3$) δ: −81.07, −114.62, −124.51, −126.06.

HRMS (EI): The molecular weight for $C_{20}H_{20}F_9N_2O_2$ $[M + H^+]$ was calculated as 491.1381, but was found as 491.1389.

The chemical structure of compound DR257 is given in Fig. 21 and the other details of synthesis follow:

6 (0.220 g, 0.449 mmol), **4** (0.048 g, 1.03 mmol), and triphenylphosphine (0.129 g, 0.490 mmol) were dissolved in dry THF (10 mL) under argon. Diethyl azodicarboxylate (0.085 g, 0.490 mmol) was dissolved in dry THF (4 mL) under argon before being added dropwise to the reaction flask. The flask was stirred overnight and then concentrated. The product was purified by column chromatography (ethyl acetate: hexane, 1.5:9, where $R_f = 0.60$ in ethyl acetate: hexane, 3:7) to yield a white powder (0.82 g, 0.140 mmol, 34%).

^{1}H NMR (400 MHz, $CDCl_3$) δ: 8.65 (s, 2H), 7.42 (m, 2H), 7.01 (m, 2H), 4.39 (t, J = 6.5, 2H), 4.23 (dd, J = 11.1, 3.3, 1H), 4.01 (dd, J = 11.1, 5.5, 1H), 3.12 (m, 1H), 2.97 (m, 1H), 2.06 (m, 2H), 1.90–1.80 (m, 2H), 1.69–1.40 (m, 10H), 0.98 (t, J = 7.3, 3H).

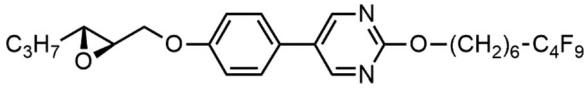

FIG. 21. Chemical structure of compound DR257.

^{13}C NMR (101 MHz, $CDCl_3$) δ: 164.63 (C), 158.94 (C), 157.09 (2CH), 128.08 (C), 127.87 (2CH), 127.56 (C), 115.70 (2CH), 68.81 (CH_2), 67.72 (CH_2), 56.61 (CH), 56.20 (CH), 33.81 (CH_2), 30.91 (t, J = 22.3, CH_2), 29.02 (CH_2), 28.84 (CH_2), 25.88 (CH_2), 20.25 (t, J = 3.7, CH_2), 19.41 (CH_2), 14.06 (CH_3).

^{19}F NMR (376 MHz, $CDCl_3$) δ: −81.08, −114.63, −124.52, −126.08.

HRMS (EI): m/z calculated for $C_{26}H_{30}F_9N_2O_3$ [M + H^+] 589.2097, found 589.2104.

$[\alpha]_D^{20}$: +8.868 (c 0.0106, $CHCl_3$).

[1] N. A. Clark and S. T. Lagerwall, Appl. Phys. Lett. **36**, 899 (1980).

[2] S. T. Lagerwall, *Ferroelectric and Antiferroelectric Liquid Crystals* (Wiley-VCH, Weinheim, 1999).

[3] T. P. Rieker, N. A. Clark, G. S. Smith, D. S. Parmar, E. B. Sirota, and C. R. Safinya, Phys. Rev. Lett. **59**, 2658 (1987).

[4] J. P. Lagerwall and F. Giesselmann, Chem. Phys. Chem. **7**, 20 (2006).

[5] M. V. Gorkunov, F. Giesselmann, J. P. F. Lagerwall, T. J. Sluckin, and M. A. Osipov, Phys. Rev. E **75**, 060701 (2007).

[6] M. V. Gorkunov, M. A. Osipov, J. P. F. Lagerwall, and F. Giesselmann, Phys. Rev. E **76**, 051706 (2007).

[7] K. Saunders, D. Hernandez, S. Pearson, and J. Toner, Phys. Rev. Lett. **98**, 197801 (2007).

[8] K. Saunders, Phys. Rev. E **77**, 061708 (2008).

[9] V. Swaminathan, V. P. Panov, Yu. P. Panarin, S. P. Sreenilayam, J. K. Vij, A. Panov, D. Rodriguez-Lojo, P. J. Stevenson, and E. Gorecka, Liq. Cryst. (2017), doi:10.1080/02678292.2017.1359694.

[10] H. G. Yoon, D. M. Agra-Kooijman, K. Ayub, R. P. Lemieux, and S. Kumar, Phys. Rev. Lett. **106**, 087801 (2011); D. M. Agra-Kooijman, H. G. Yoon, S. Dey, and S. Kumar, Phys. Rev. E **89**, 032506 (2014).

[11] Y. Gao, J. M. Klunder, R. M. Hanson, H. Masamune, S. Y. Ko, and K. B. Sharpless, J. Am. Chem. Soc. **109**, 5765 (1987); Y. Tu, Z. Wang, and Y. Shi, *ibid.* **118**, 9806 (1996).

[12] D. Nonnenmacher, M. A. Osipov, J. C. Roberts, R. P. Lemieux, and F. Giesselmann, Phys. Rev. E **82**, 031703 (2010).

[13] C. P. J. Schubert, C. Muller, F. Giesselmann, and R. P. Lemieux, J. Mater. Chem. C **4**, 8483 (2016).

[14] J. C. Roberts, N. Kapernaum, Q. Song, D. Nonnenmacher, K. Ayub, F. Giesselmann, and R. P. Lemieux, J. Am. Chem. Soc. **132**, 364 (2010).

[15] C. P. J. Schubert, A. Bogner, J. H. Porada, K. Ayub, T. Andrea, F. Giesselmann, and R. P. Lemieux, J. Mater. Chem. C **2**, 4581 (2014).

[16] A. de Vries, J. Chem. Phys. **71**, 25 (1979).

[17] G. W. Gray and J. W. Goodby, *Smectic Liquid Crystals* (Leonard Hill, London, 1984).

[18] A. de Vries, Mol. Cryst. Liq. Cryst. **41**, 27 (1977).

[19] J. W. Goodby, in *Handbook of Liquid Crystals*, 2nd ed., edited by J. W. Goodby, P. J. Collings, T. Kato, C. Tschierske, H. F. Gleeson, and P. Raynes (Wiley-VCH, 2015), Vol. 1, Chap. 3.

[20] J. Naciri, G. P. Crawford, B. R. Ratna, and R. Shashidhar, Ferroelectrics **148**, 297 (1993).

[21] Y. Takanishi, Y. Ouchi, H. Takezoe, A. Fukuda, A. Mochizuki, and M. Nakatsuka, Jpn. J. Appl. Phys. **29**, L984 (1990).

[22] L. Li, C. D. Jones, J. Magolan, and R. P. Lemieux, J. Mater. Chem. **17**, 2313 (2007).

[23] B. Park, S. -S. Seomun, M. Nakata, and M. Takahashi, Jpn. J. Appl. Phys. **38**, 1474 (1999).

[24] V. M. Vaksman and Yu. P. Panarin, Mol. Mater. **1**, 147 (1992); V. Panov, J. K. Vij, and N. M. Shtykov, Liq. Cryst. **28**, 615 (2001).

[25] S. Inui, N. Iimura, T. Suzuki, H. Iwane, K. Miyachi, Y. Takanishi, and A. Fukuda, J. Mater. Chem. **6**, 671 (1996).

[26] S. Garoff and R. B. Meyer, Phys. Rev. Lett. **38**, 848 (1977).

[27] N. A. Clark, T. Bellini, R.-F. Shao, D. Coleman, S. Bardon, D. R. Link, J. E. Maclennan, X.-H. Chen, M. D. Wand, D. M. Walba, P. Rudquist, and S. T. Lagerwall, Appl. Phys. Lett. **80**, 4097 (2002).

[28] Y. Shen, L. Wang, R. Shao, T. Gong, C. Zhu, H. Yang, J. E. Maclennan, D. M. Walba, and N. A. Clark, Phys. Rev. E **88**, 062504 (2013).

[29] S. T. Lagerwall, P. Rudquist, and F. Giesselmann, Mol. Cryst. Liq. Cryst. **510**, 148 (2009).

[30] J. V. Selinger, P. J. Collings, and R. Shashidhar, Phys. Rev. E **64**, 061705 (2001).

[31] R. Qiu, J. T. Ho, and S. K. Hark, Phys. Rev. A **38**, 1653 (1988).

[32] F. Giesselmann, P. Zugenmaier, I. Dierking, S. T. Lagerwall, B. Stebler, M. Kaspar, V. Hamplova, and M. Glogarova, Phys. Rev. E **60**, 598 (1999).

[33] O. E. Panarina, Yu. P. Panarin, J. K. Vij, M. S. Spector, and R. Shashidhar, Phys. Rev. E **67**, 051709 (2003).

[34] K. L. Sandhya, Yu. P. Panarin, V. P. Panov, J. K. Vij, and R. Dabrowski, Eur. Phys. J. E **27**, 397 (2008).

[35] P. G. de Gennes and J. Prost, *The Physics of Liquid Crystals* (Clarendon, Oxford, 1993), Chap. 10, p. 514.

[36] S. Havriliak, Jr. and S. Negami, Polymer **8**, 161 (1967).

[37] O. E. Kalinovskaya and J. K. Vij, J. Chem. Phys. **111**, 10979 (1999).

[38] U. Manna, J.-K. Song, Yu. P. Panarin, A. Fukuda, and J. K. Vij, Phys. Rev. E **77**, 041707 (2008).

[39] S. P. Sreenilayam, D. M. Agra-Kooijman, V. P. Panov, V. Swaminathan, J. K. Vij, Yu. P. Panarin, A. Kocot, A. Panov, D. Rodriguez-Lojo, P. J. Stevenson, M. R. Fisch, and S. Kumar, Phys. Rev. E **95**, 032701 (2017).

[40] N. Yadav, V. P. Panov, V. Swaminathan, S. P. Sreenilayam, J. K. Vij, T. S. Perova, R. Dhar, A. Panov, D. Rodriguez-Lojo, and P. J. Stevenson, Phys. Rev. E **95**, 062704 (2017).

[41] H. Xu, J. K. Vij, A. Rappaport, and N. A. Clark, Phys. Rev. Lett. **79**, 249 (1997).

[42] A. Kocot, R. Wrzalik, J. K. Vij, and R. Zentel, J. Appl. Phys. **75**, 728 (1994).

[43] J. Q. Huang, W. D. Meng, and F. L. Qing, J. Fluor. Chem. **128**, 1469 (2007).